

Single π^0 Production Off Neutrons Bound in Deuteron with Linearly Polarized Photons

C. Mullen¹, S. Gardner¹, D. I. Glazier^{a,1}, S. J. D. Kay^{2,3}, K. Livingston¹, I. I. Strakovsky⁴,
R. L. Workman⁴, S. Abt⁵, P. Achenbach⁶, F. Afzal⁷, Z. Ahmed³, C. S. Akondi⁹,
J. R. M. Annand¹, M. Bashkanov¹⁴, R. Beck⁹, M. Biroth⁶, N. S. Borisov⁹, A. Braghieri⁸,
W. J. Briscoe⁴, F. Cividini⁶, C. Collicott⁶, S. Costanza⁸, A. Denig⁶, M. Dieterle⁵, E. J. Downie⁴,
P. Drexler⁶, S. Fegan¹⁴, M. I. Ferretti-Bondy⁶, D. Ghosal⁵, I. Gorodnov⁹, W. Gradl⁶,
M. Günther⁵, G. Gurevic¹¹, L. Heijdenskjöld⁶, D. Hornidge¹³, G. M. Huber³, N. Jermann⁵,
A. Kaeser⁵, M. Korolija¹⁵, V. L. Kashevarov⁶, B. Krusche⁵, V. V. Kulikov¹⁶, A. Lazarev⁷,
S. Lutterer⁵, I. J. D. MacGregor¹, D. M. Manley⁹, P. P. Martel⁶, M. A. Martemianov¹⁶,
C. Meier⁵, R. Miskimen¹⁰, M. Mocanu¹⁴, E. Mornacchi⁶, A. Neganov⁹, M. Oberle⁵, M. Ostrick⁶,
P. Otte⁶, D. Paudyal³, P. Pedroni⁸, A. Powell¹, S. N. Prakhov⁶, G. Reicherz¹⁷, G. Ron¹²,
T. Rostomyan⁵, C. Sfienti⁶, V. Sokhoyan⁶, K. Spieker⁷, O. Steffen⁶, Th. Strub⁵, I. Supek¹⁵,
A. Thiel⁷, M. Thiel⁶, A. Thomas⁶, M. Unverzagt⁶, Yu. A. Usov⁹, S. Wagner⁶, N. K. Walford⁵,
D. P. Watts¹⁴, D. Werthmüller¹, J. Wettig⁶, L. Witthauer⁵, M. Wolfes⁶, N. Zachariou¹⁴
(A2 Collaboration at MAMI)

¹ SUPA, School of Physics and Astronomy, University of Glasgow, Glasgow G12 8QQ, UK

² SUPA, School of Physics and Astronomy, University of Edinburgh, Edinburgh EH9 3FD, UK

³ Department of Physics, University of Regina, Regina, SK S4S 0A2, Canada

⁴ Department of Physics, Institute for Nuclear Studies, The George Washington University, Washington, DC 20052, USA

⁵ Institut für Physik, University of Basel, Basel CH-4056, Switzerland

⁶ Institut für Kernphysik, Johannes Gutenberg-University Mainz, D-55099 Mainz, Germany

⁷ Helmholtz-Institut für Strahlen- und Kernphysik, University of Bonn, Bonn D-53115, Germany

⁸ INFN Sezione di Pavia, I-27100 Pavia, Italy

⁹ Kent State University, Kent, OH 44242, USA JINR, 141980 Dubna, Russia

¹⁰ University of Massachusetts, Amherst, MA 01003, USA

¹¹ Institute for Nuclear Research, 125047 Moscow, Russia

¹² Racah Institute of Physics, Hebrew University of Jerusalem, Israel

¹³ Mount Allison University, Sackville, NB E4L3B5, Canada

¹⁴ Department of Physics, University of York, Heslington, York YO10 5DD, UK

¹⁵ Rudjer Boskovic Institute, Zagreb HR-10000, Croatia

¹⁶ NRC "Kurchatov Institute" - ITEP, Moscow 117218, Russia

¹⁷ Institut für Experimentalphysik, Ruhr-University of Bochum, Bochum D-44801, Germany

Received: date / Accepted: date

Abstract The quasifree $\vec{\gamma}d \rightarrow \pi^0 n(p)$ photon beam asymmetry, Σ , has been measured at photon energies, E_γ , from 390 to 610 MeV, corresponding to center of mass energy from 1.271 to 1.424 GeV, for the first time. The data were collected in the A2 hall of the MAMI electron beam facility with the Crystal Ball and TAPS calorimeters covering pion center-of-mass angles from 49 to 148°. In this kinematic region, polarization observables are sensitive to contributions from the $\Delta(1232)$ and $N(1440)$ resonances. The extracted values of Σ have been compared to predictions based on partial-wave analyses (PWAs) of the existing pion photopro-

duction database. Our comparison includes the SAID, MAID, and Bonn-Gatchina analyses; while a revised SAID fit, including the new Σ measurements, has also been performed. In addition, isospin symmetry is examined as a way to predict $\pi^0 n$ photoproduction observables, based on fits to published data in the channels $\pi^0 p$, $\pi^+ n$, and $\pi^- p$.

PACS 13.60.Le Meson production · 13.88.+e Polarization in interactions and scattering

^ae-mail: Derek.Glazier@glasgow.ac.uk

1 Introduction

Knowledge of the N^* and Δ^* resonance decay couplings to nucleons and photons is largely restricted to charged states. Increasing the body of neutron-target measurements will allow a more highly constrained study of neutral states and their $n\gamma$ couplings. The four charge channels ($\pi^0 p$, $\pi^+ n$, $\pi^- p$, and $\pi^0 n$) of pion photoproduction can be described in terms of three isospin amplitudes. This gives the possibility of predicting properties of one channel based on sufficiently detailed measurements of the other three. The $\pi^0 n$ channel is the least-studied and was the subject of this experiment.

Most existing γn data are unpolarized and provide around 1900 $\pi^0 n$ photoproduction data points, spanning the full nucleon resonance region [1] (Table 1). The $\vec{\gamma} n \rightarrow \pi^0 n$ beam asymmetry, Σ , was previously measured by the GRAAL Collaboration [10]. The beam asymmetry measures the relative strength of the production with respect to the plane of photon linear polarisation. Their measurements covered beam energy, E_γ , from 703 to 1475 MeV, corresponding to a centre-of-mass energy, W , range from 1.484 to 1.912 GeV, just above the current results.

Recently, the A2 Collaboration at MAMI published high-quality unpolarized measurements for π^0 photoproduction off a neutron below $E_\gamma = 813$ MeV [4]. The present data extend the range of the previous GRAAL polarized measurements [10], for $\pi^0 n$ photoproduction. Further A2 Collaboration measurements of the $\pi^0 n$ E asymmetry, with longitudinal polarized target and circularly polarized photons, for $E_\gamma = 216 - 1606$ MeV [12], extend previous A2 $\pi^0 n$ E measurements [11]. These data will provide the basis for better-constrained γn decay amplitudes in the near future.

Apart from lower-energy inverse reaction $\pi^- p \rightarrow \gamma n$ measurements, the extraction of the two-body $\gamma n \rightarrow \pi^- p$ and $\gamma n \rightarrow \pi^0 n$ observables requires the use of a model-dependent nuclear correction, which mainly comes from final-state interaction (FSI) effects. In several papers, the GWU-ITEP group have shown that the FSI corrections on unpolarized cross sections are less than 20% (see, for instance, Refs. [13–15]). As polarization asymmetries measure ratios of cross sections, FSI effects are expected to have a considerably smaller effect on these, including Σ , and will be comparable, or less than our quoted systematic uncertainties from experimental sources. In this publication, Σ for the neutron bound in a deuteron is presented uncorrected for potential FSI effects so as not to add any model dependence to the results.

The organization for this paper is as follows. In Section 2, details of the A2 experiment and detectors are

given; Section 3 outlines the event selection; Section 4 reviews the background subtraction; Section 5 covers the determination of the photon asymmetry; and Section 6 outlines the dominant sources of systematic uncertainty; Section 7 outlines the PWA methods used in the fits and predictions compared to data. Finally, Section 8 presents the results and interpretation of the present A2 Σ data.

2 Experiment

The reaction $\vec{\gamma} d \rightarrow \pi^0 n(p)$ was measured at the Mainzer Microtron (MAMI) electron accelerator facility, in August 2016. The 1.5 GeV MAMI electron beam, incident on an aligned diamond radiator, produced a photon beam via coherent bremsstrahlung, with significant linear polarization up to photon energies of 610 MeV. The energy of the photon beam was measured using the Glasgow-Mainz Tagged Photon Spectrometer with a resolution of around 4 MeV. This spectrometer measured the position of the degraded post-bremsstrahlung electron on a plastic scintillator focal plane consisting of 353 elements after traversing a 1.8 T magnetic dipole field [16]. The energy of the detected electron, and therefore also the energy of the photon, was deduced from this position.

The photon beam interacted in a 10 cm long liquid deuterium target (LD_2). The reaction products were detected in two calorimeters: the Crystal Ball (CB), a highly segmented array of 672 NaI(Tl) crystals arranged in a sphere centered on the target cell [17]; and the TAPS calorimeter, a forward wall of 366 BaF₂ and 72 PbWO₄ crystals arranged 1.5 m downstream from the CB center [18] (Fig. 1). The CB covers lab. frame angles $21^\circ < \theta_L < 159^\circ$ and TAPS approximately $2^\circ < \theta_L < 20^\circ$. The LD_2 target cell was surrounded by a Particle Identification Detector (PID) consisting of 24, 30 cm long plastic scintillators arranged in a cylindrical formation. This allowed separation of reactions with a scattered neutron from those with a proton. A Multi-Wire Proportional Chamber barrel (MWPC) provided tracking information for charged particles which were not used for the all-neutral final state investigated here, however here they provided additional proton rejection. Charge particle identification was provided in the case of the TAPS detector by a thin plastic veto layer in front of each crystal. In addition, a 2.6 cm thick graphite cylinder was situated between the PID and the MWPC to be used as the analysing material for a nucleon polarimeter [19], and was not required for this analysis [20].

Table 1 Published data for $\gamma n \rightarrow \pi^0 n$ reaction as given in the SAID database [2]: 1st column is the observable, 2nd column is the number of energy bins, 3rd column is the number of data points.

Observable	Nexp	Ndata	$E_\gamma(\text{min})$ (MeV)	$E_\gamma(\text{max})$ (MeV)	$\theta(\text{min})$ ($^\circ$)	$\theta(\text{max})$ ($^\circ$)	Laboratory	Ref
$d\sigma/d\Omega$	9	9	208	373	147	148	MAMI	[3]
	27	492	290	813	18	162	MAMI	[4]
	40	43	299	889	70	130	Tokyo	[5]
	49	931	446	1427	32	162	MAMI	[6]
	42	42	455	905	45	143	Tokyo	[7]
	35	35	462	784	60	135	Frascati	[8]
	3	28	911	1390	3	91	SLAC	[9]
Σ	27	216	703	1475	53	164	GRAAL	[10]
E	17	151	446	1427	46	154	MAMI	[11]

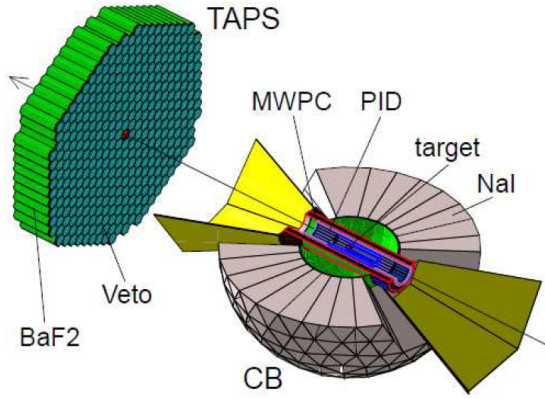


Fig. 1 Set-up of the A2 experiment. CB shows a NaI(Tl) calorimeter, TAPS shows a BaF₂ and PbWO₄ calorimeter, PID shows a plastic scintillator detector for particle identification, MWPC are two cylindrical multiwire proportional chambers, and target shows the liquid deuterium target LD_2 (see text for details).

All simulations used in this analysis were performed with a full detector model using the Geant4 [33] toolkit.

The linear polarization of the photons was produced by coherent bremsstrahlung [21, 22], with the electron beam scattered coherently from an aligned radiator. A thin diamond crystal (30 μm) with low mosaic-structure was used to minimize the energy smearing of the coherent spectrum arising from electron multiple scattering effects and crystal defects in the lattice [23]. The alignment of the diamond was carried out using the Stonehenge technique [24] with two orthogonal polarization plane orientations chosen to be at azimuthal angles of $\pm 45^\circ$ with respect to the equatorial plane of the CB detector. To increase the degree of linear polarization a 2 mm diameter Pb-collimator was installed

2.5 m downstream of the radiator, enhancing the ratio of coherent to incoherently scattered photons that reached the LD_2 . The degree of linear polarization was determined by calibrating against the linearly polarized photon beam asymmetry for π^0 production off the proton. This was measured for each photon energy bin and compared to a recent SAID PWA solution including recent high statistics measurements in the same energy range [25]. The ratio of the measured asymmetry to the SAID values gave the photon polarization for each energy bin. The analysis of the proton asymmetry was performed in the same manner as the neutron asymmetry described here. The resulting photon polarization ranged from 15% at $E_\gamma = 390$ MeV to a maximum of 55% at 610 MeV [20].

3 Data Analysis

The photon asymmetry, Σ , for the reaction $\gamma d \rightarrow \pi^0 n(p)$ has been measured for beam energies in the range 390 – 610 MeV and a center-of-mass (c.m.) production angle, θ , range of $49^\circ - 148^\circ$. The semi-inclusive final state of interest included the recoiling neutron and π^0 , and omitted the spectator proton. It was identified by detecting three neutral particles, two γ s stemming from the decay of the π^0 , and a neutron as the third. The energy of the three particles was measured by the CB and TAPS calorimeters which, in coincidence with a tagged photon, allowed the reaction to be reconstructed. The classification of a neutral state was made if there were no hits in the PID or MWPC detectors for the CB or the TAPS veto layer. The spectator proton was not considered as it typically did not have sufficient energy to reach the calorimeters. The π^0 was reconstructed from the combination of two of the three particles detected. All combinations were considered, and any incorrect 2γ combinations were removed, either by subsequent cuts or by background subtraction.

Table 2 A summary of the loose cuts applied to the data before the sPlots fits.

Variable	Cut Range	Units
Tagged Time	$-80 < t_{\pi^0} < 20$	ns
Coplanarity	$-50 < \Delta\phi < 50$	degree
Missing Mass	$1850 < M_{\text{miss}} < 2300$	MeV/c ²
Cone Angle	$0 < \theta_{\text{Cone}} < 0.5$	radian
Invariant Mass	$80 < M_{\text{inv}} < 200$	MeV/c ²
Spectator Momentum	$0 < P_{\text{spec}} < 200$	MeV/c

Preliminary cuts were placed on a number of variables. These were guided by simulated signal and background channels to ensure no actual signal was lost and are given in Table 2. The missing mass was constructed using the mass of the missing 4-momentum defined as:

$$P_{\text{miss}} = P_{\text{beam}} + P_d - P_{\pi^0}, \quad (1)$$

where P_{beam} is the 4-momentum for the beam photon, P_d is the 4-momentum of the stationary deuterium target, and P_{π^0} is the 4-momentum of the detected π^0 . The mass of this missing 4-momentum gave a peak distributed around the summed mass of the two nucleons with some extra smearing from initial Fermi motion within the deuteron. When this initial momentum was low, as was generally the case, the resulting spectator proton momentum was also low and the reaction was approximately two-body with the π^0 and participant nucleon being nearly coplanar in ϕ :

$$\Delta\phi = \phi_{\pi^0} - \phi_{n-180^\circ} \sim 0^\circ, \quad (2)$$

where ϕ_{π^0} is the reconstructed azimuthal angle of the π^0 and ϕ_{n-180° the azimuthal angle of the detected neutron after rotation by 180° around the z-axis.

The detection of the π^0 and the neutron allowed the construction of the difference between the detected nucleon polar angle and the nucleon polar angle reconstructed from the π^0 assuming a stationary initial state neutron. This gives the definition of the ‘‘Cone Angle’’, θ_{Cone} .

The momentum of the spectator proton was also used to distinguish the quasi-free final state. It was calculated via:

$$P_{\text{spec}} = P_{\text{beam}} + P_d - P_{\pi^0} - P_n, \quad (3)$$

where P_n is the 4-momentum of the detected participant nucleon. The magnitude of momentum for the participant nucleon was calculated using conservation of momentum and energy in the three-body final state, using the measured π^0 momentum and the neutron direction, as given by its cluster hit position in the CB.

4 Background Subtractions

To further isolate the true $\pi^0 n$ final state, several sources of background had to be subtracted from the selected events. The main sources of these backgrounds were: random electrons in the photon tagger; background to the two photon combination giving the π^0 ; and other reactions producing the same detected particles as the $\pi^0 n(p)$ reaction. The sPlot technique was used to remove these background events using a separate discriminatory variable for each source to produce event-by-event weights termed sWeights, for full details see [26]. The sWeights are normalized using the relative yields and covariance matrix of the signal and background derived from the fits. Weights corresponding to regions of high background are negative and effectively subtract off this contribution to the distribution. This is similar to how a ‘‘sideband subtraction’’ method works, but is more generally applicable. Consecutive fits were performed applying the sWeights from the previous fit. An sPlot fit to the discriminatory variables using appropriate probability density functions (PDFs) derived from simulated event samples, determined the yields of the different event species. The covariance matrix of this yield fit was then used to calculate the sWeights associated with each event in the fitted sample. Including these sWeights in the subsequent observable fits allowed determination of the photon asymmetry for our signal. The fits to the discriminatory variables are described in the following sections.

4.1 Random Tagged Photons

Random coincidences with background electrons in the photon tagger were removed via the coincidence time between the π^0 and the tagged beam photon as given by:

$$t_{\text{coin}} = \frac{t_{\gamma 1} + t_{\gamma 2}}{2} - t_{\text{tagger}}, \quad (4)$$

with the time of the electron in the tagger, t_{tagger} and the time in the calorimeters of the 2 photons $t_{\gamma 1,2}$. This resulted in a timing distribution strongly peaked at zero with a flat random background, as shown in Fig. 2 for the bin $E_\gamma = 610$ MeV and $\cos\theta_{CM} = 0.05$. In this case, a Gaussian PDF was used for the signal with a uniform background function.

4.2 Background in 2γ Invariant Mass

Background to real π^0 decays in the two γ invariant mass distribution can arise from a wrong combination of the three neutral clusters, or multiple clusters created

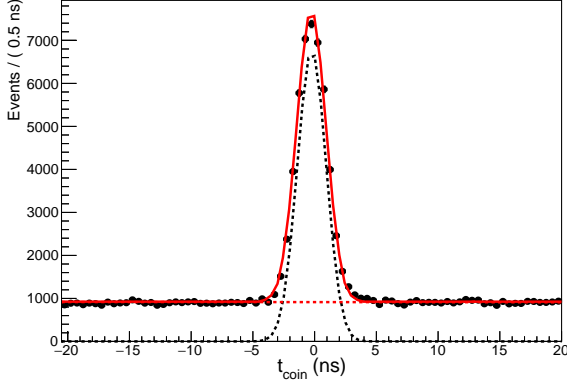


Fig. 2 The timing coincidence spectra between the photon beam tagger and the calorimeters. Black points are data; red solid line is full fit result; dashed black is signal Gaussian function; dashed red is flat background function. This fit was used to produce weights to subtract the random background events.

by one actual particle. These background sources will not give a peaking structure in the invariant mass distribution and were thus subtracted using the sPlot technique. The π^0 signal PDF was taken from a histogram template of simulated events, while the background was modelled by a third order Chebychev polynomial. An example fit is shown for the bin $E_\gamma = 610$ MeV and $\cos \theta = 0.05$ in Fig. 3. In this mass range, the π^0 signal was typically around 90% of the total events.

4.3 Background to the $\pi^0 n(p)$ final state

Background to the final state may come, for example, from events in which more than one pion is produced. This background is reduced with the loose cuts given in Table 2. To determine the sWeights for subtracting the residual background, the coplanarity given in Eq. 2 was used. The signal PDF shape was given by simulated data and the background by a second order Chebychev polynomial. The resulting fit, for the bin $E_\gamma = 610$ MeV and $\cos \theta = 0.05$, is shown in Fig. 4.

5 Determination of the Photon Asymmetry

The photon asymmetry, Σ , quantifies the effect of the polarization of the beam on the excitation of the neutron and its subsequent decay to a pion and nucleon. With a linearly polarized photon beam the differential cross section is

$$\frac{d\sigma}{d\Omega} = \left(\frac{d\sigma}{d\Omega} \right)_0 (1 + P_L \Sigma \cos 2\phi), \quad (5)$$

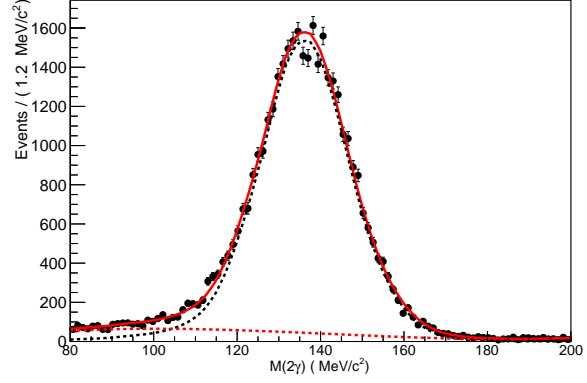


Fig. 3 The invariant mass of the two detected γ s. Black points are data; red solid line is full fit result; dashed black is simulated signal function; dashed red is third degree Chebychev polynomial. This fit was used to produce weights to subtract background events that did not have a π^0 .

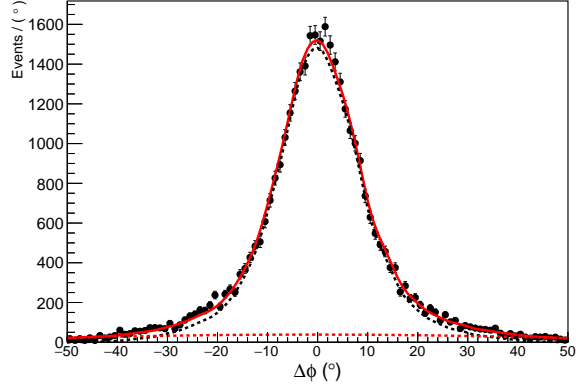


Fig. 4 The coplanarity between the π^0 and detected neutron. Black points are data; red solid line is full fit result; dashed black is simulated signal function; dashed red is second degree Chebychev polynomial. This fit was used to produce weights to subtract events that did not originate from the $\vec{\gamma}d \rightarrow \pi^0 n(p)$ final state.

where ϕ is the azimuthal angle of the meson production plane relative to the plane of linear polarization and P_L is the degree of linear polarization. Rotating the orientation of the diamond radiator allowed the plane of linear polarization to flip between $-\frac{\pi}{4}$ and $\frac{\pi}{4}$. Shifting the plane by $\frac{\pi}{2}$ effectively flips the sign of the asymmetry giving two polarization states $P_S = \pm 1$.

To extract Σ from the measured ϕ distributions unbinned extended maximum likelihood fits were performed. The fit function was given by

$$F(\Sigma : \phi, P_S, P_L) = 1 + \Sigma P_S P_L \cos(2\phi + \phi_0), \quad (6)$$

with ϕ_0 determined from fits to be 95.8° .

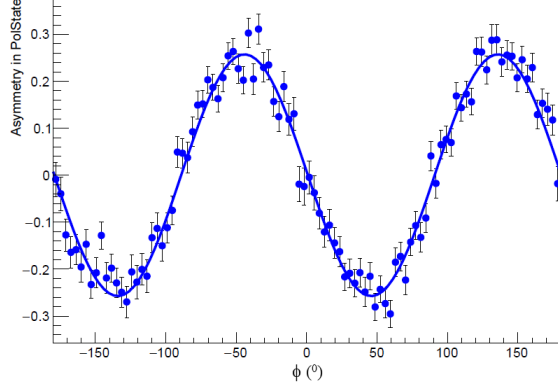


Fig. 5 Example of fitted asymmetry used to extract Σ . Blue points are the data and blue solid line is the result of the maximum likelihood fit.

The negative log likelihood function given by

$$-\ln L = -\sum_i^N w_i \ln F(\Sigma : \phi_i, P_{S,i}, P_{L,i}) + B(\Sigma), \quad (7)$$

was minimized using Minuit as part of the ROOFIT [27] library. Here, N is the number of data events in the E_γ and θ bin, while subscript i refers to the value of the variables for a given event. In particular, w_i represents the value of the sWeight used to subtract background events from the likelihood summation.

The PDF normalization integral term $B(\Sigma)$ was determined by Monte-Carlo integration using simulated data. For this, P_S and P_L values were randomly chosen to match the fluxes and polarization degrees of the real data. This effectively corrected for second order systematic effects due to differences in polarization state luminosity and degree of polarization.

An example of the resulting fitted asymmetry in polarization state compared to the background subtracted data asymmetry, where the plotted asymmetry is calculated as,

$$A(\phi) = \frac{F(\phi : P_S = +1) - F(\phi : P_S = -1)}{F(\phi, P_S = +1) + F(\phi, P_S = -1)} \quad (8)$$

is shown in Fig. 5, for the bin $E_\gamma = 610$ MeV and $\cos\theta = 0.05$, as an illustration. The fits were performed in bins of 20 MeV for E_γ and 0.1 in $\cos\theta$. Results are shown in Fig. 6 alongside solutions of various PWAs described in Section 7.

6 Systematic Uncertainties

The dominant sources of systematic uncertainty in the results came from the linear polarization calibration and the background subtraction. The fractional difference between a simple cuts-based analysis and the sPlot

background subtraction methods gave an estimate of the systematic uncertainty in background subtraction method for each point. For the cuts-based analysis a similar procedure was performed but, rather than use a sPlot subtraction, tighter cuts were placed on the discriminatory variables to identify a cleaner sample of $n\pi^0$ events with residual backgrounds estimated by simulations to be around 3.6%. These cuts are summarised in Table 3. While a cuts-only analysis retains some

Table 3 A summary of the tight cuts applied to the data to produce a low background event sample.

Variable	Cut Range	Units
Tagged Time	$-5 < t_{\pi^0} < 5$	ns
Coplanarity	$-30 < \Delta\phi < 30$	degree
Missing Mass	$1850 < M_{\text{miss}} < 2100$	MeV/c ²
Cone Angle	$0 < \theta_{\text{Cone}} < 0.3$	radian
Invariant Mass	$110 < M_{\text{inv}} < 160$	MeV/c ²
Spectator Momentum	$0 < P_{\text{spec}} < 200$	MeV/c

small amount of background, as illustrated in Figs. 3 and 4, the sPlot method is expected to remove all the background. Any error in the subtraction of the background by the weights-based method is expected to be less than the effect of not subtracting the background. Hence, the difference between Σ extracted from the cuts and sPlot subtracted results is used as a conservative estimate of this systematic uncertainty [20]. Values for this systematic uncertainty were calculated for each E_γ and θ bin with a mean value of 3%. For the systematic uncertainty in the degree of linear polarization there are two factors, first the uncertainty in the SAID solution for Σ on $p\pi^0$, which was used to determine the polarization, and was estimated to be 2%. Second, the uncertainty on our extraction of the $p\pi^0$ asymmetries which had a main contribution from the background subtraction which was estimated in a similar manner to the $n\pi^0$ background subtraction and found to be 4%. Adding these two factors in quadrature gives an overall 4.5% systematic uncertainty in our Σ results due to the linear polarization. Other uncertainties were found to be much smaller than these sources: acceptance effects, such as the neutron detection efficiency, cancel due to the polarization flip; polarization degree and luminosity asymmetries were incorporated into the likelihood fit; and unbinned fits were used, removing binning artifacts from the results.

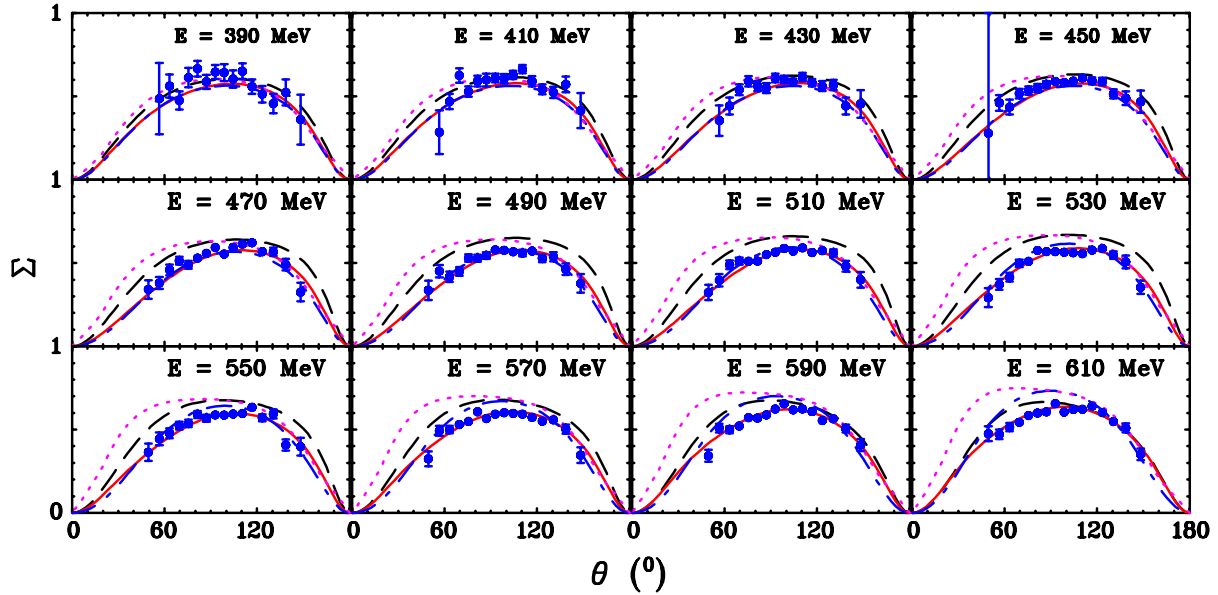


Fig. 6 Σ for $\bar{\gamma}n \rightarrow \pi^0 n$ vs. pion production angle θ in c.m. frame: A2 (blue filled circles); fit: SAID MU22 (red solid curves), SAID MA19 [4] (blue dash-dotted curves), Bonn-Gatchina BG2014-02 [28] (magenta dotted curves), and MAID2007 [29] (black dashed curves). Only angle-dependent uncertainties are shown for all data. Each plot corresponds to a 20 MeV wide bin in E_γ with the central value given in each.

7 Multipole Analysis

The SAID [30], MAID [29], and Bonn-Gatchina [31] analyses use different fit formalisms to extract the partial-wave (multipole) amplitudes underlying different data-sets. Comparing the different resulting amplitudes gives an estimate of the systematic errors inherent in the process.

For the MAID analysis, which was completed in 2007, the most recent data-sets have not been included and this must be considered when making comparisons [29]. The MAID unitary isobar approach applies a Breit-Wigner resonance plus background model, guaranteeing unitarity up to the two-pion production threshold.

The Bonn-Gatchina method fits a wider range of reactions utilizing elements of the K-matrix and P-vector approaches [31]. Both pion and photo-induced reactions are included in a multi-channel fit. Reactions with three-body final states are included using an event-based likelihood fit. The elastic pion-nucleon reaction is fitted based on existing amplitudes. The various data types are fitted with the possibility of renormalization and weighting.

The SAID method is an extension of the Chew-Mandelstam K-matrix approach used to fit pion-nucleon elastic scattering and ηN production data. The reso-

nance spectrum is fixed from this fit [32] and only the photo-couplings are allowed to vary. This differs from the MAID and Bonn-Gatchina analyses, which can add new resonances to improve the agreement with data. The formalism has built-in cuts associated with the $\pi\Delta$, ρN , and ηN thresholds but only single-pion photoproduction data are fitted. Data have been weighted and renormalized in previous fits. No weighting and only renormalization at the one percent level was utilized in fitting the present set of Σ data.

For each angular distribution, a normalization constant (X) and its uncertainty (ϵ_X) were assigned. The quantity ϵ_X is generally associated with the normalization uncertainty (if known). The modified χ^2 function to be minimized is given by

$$\chi^2 = \sum_i \left(\frac{X\eta_i - \eta_i^{exp}}{\epsilon_i} \right)^2 + \left(\frac{X - 1}{\epsilon_X} \right)^2, \quad (9)$$

where the subscript i labels the data points within the distribution, η_i^{exp} is an individual measurement, η_i is the corresponding calculated value, and ϵ_i represents the angular-dependent statistical uncertainty. The total χ^2 is then found by summing over all measurements. This re-normalization freedom is often important in obtaining the best SAID fit results. For other data analyzed in the fit, such as the total cross sections and exci-

tation data, the statistical and systematic uncertainties were combined in quadrature and no re-normalization was allowed.

In fitting the present set of Σ data, an overall angle-independent systematic uncertainty of 1% was used for ϵ_X in Eq. (9). The resulting values for X remained within ϵ_X of unity on average.

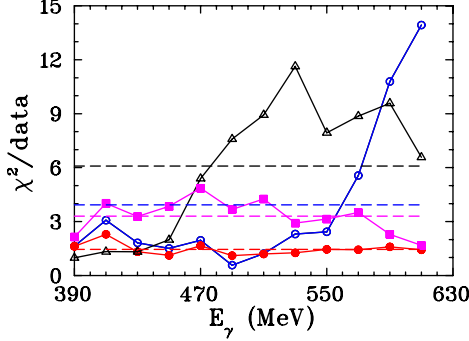


Fig. 7 Comparison of χ^2 per data point for the previous SAID solution MA19 [4] and MAID2007 [29] applied to the present A2 data with blue open circles and black open triangles, respectively. The new SAID solution MU22 (MUXX) with red full circles and magenta full squares obtained after adding the present A2 data (MUXX does not have any $\gamma n \rightarrow \pi^0 n$ data). Also shown are the fit χ^2 per data point values averaged over each energy bin E_γ , where the horizontal dashed lines are for the MU22 (red), MUXX (magenta), MA19 (blue), and MAID2007 (black) solutions. The solid lines connecting the points are included only to guide the eye.

A revised SAID multipole analysis has been completed, including the present set of $\vec{\gamma}n \rightarrow \pi^0 n$ Σ data. This new global energy-dependent solution has been labeled as MU22. The overall fit quality of the present MU22 and previous MA19 [4] SAID fits is compared with the MAID2007 [29] solution in Tables 4 and 5. The inclusion of the present A2 data set provides a fit with significantly improved χ^2/data , specifically at higher energies, in comparisons between the $\pi^0 n$ fits and data (χ^2/data for MA19 = 3.93 and χ^2/data for MU22 = 1.44) as shown in Fig. 7 and Table 4. This demonstrates the influence of these asymmetry measurements with their small uncertainties. The overall comparison of the MA19 and MU22 solutions shows that the fit χ^2/data values are essentially unchanged for $\pi^0 p$ and $\pi^+ n$ channels. The χ^2 per data point including all available data and the present A2 data for MA19 and MU22 (with MAID2007) is given in Table 5.

Additionally, an alternative MUXX solution was generated excluding all world $\gamma n \rightarrow \pi^0 n$ data and show results in Fig. 8 and Table 4. The excellent comparison of the isospin-predicted Σ to the data strongly suggests

Table 4 χ^2 per data point for new A2 data. Predictions are from MAID2007 [29] and the SAID fit MUXX (no world $\pi^0 n$ data fitted), an older SAID fit to existing data (MA19 [4]), and the SAID fit including present data (MU22).

Solution	$\chi^2/(\pi^0 n \text{ data})$
MU22	275/189=1.46
MUXX	624/189=3.30
MA19	743/189=3.93
MAID2007	1151/189=6.09

the systematics in the new data are well under control. The comparisons with MAID are interesting as both solutions use isospin symmetry to predict the $\pi^0 n$ observables based on the available data from the other three charge channels in 2007 and 2020.

Table 5 χ^2 per data point values for all charge channels covering the energy range from 155 MeV to 1000 MeV. Fits as described in Table 4.

Solution	$\chi^2/(\pi^0 p \text{ data})$	$\chi^2/(\pi^+ n \text{ data})$
MU22	13274/9534=1.39	7454/4039=1.85
MUXX	13171/9534=1.38	7259/4039=1.80
MA19	12565/9534=1.32	7461/4039=1.85
MAID2007	73638/9534=7.72	14599/4039=3.61
Solution	$\chi^2/(\pi^0 n \text{ data})$	$\chi^2/(\pi^- p \text{ data})$
MU22	2345/ 798=2.94	5879/3456=1.70
MUXX	7639/ 798=9.57	5384/3456=1.56
MA19	2649/ 798=3.32	5999/3456=1.74
MAID2007	4846/ 798=6.07	15365/3456=4.45

8 Results and Interpretation

A comprehensive set of Σ data for $\vec{\gamma}d \rightarrow \pi^0 n(p)$ at 12 photon energies has been determined with the CB and TAPS spectrometers using a tagged photon beam at incident photon energies from 390 to 610 MeV. The present Σ data cover the resonance region from above the maximum of the Δ -isobar to the Roper resonance.

The SAID MA19 [4], Bonn-Gatchina BG2014-02 [28], and MAID2007 [29] curves shown in Fig. 6 did not include the present A2 data in their fits. In addition, the MAID2007 fit does not include measurements after 2007. MU22 includes all previous measurement and includes the A2 data. All fits and predictions agree well for the lowest energy where the Δ resonance dominates. The angular distribution retains the shape of SAID MA19 up until the highest energies where some larger deviations become apparent.

Exploring the effectiveness of isospin symmetry to predict $\pi^0 n$ observables, in Fig. 8 the fit (MU22) is

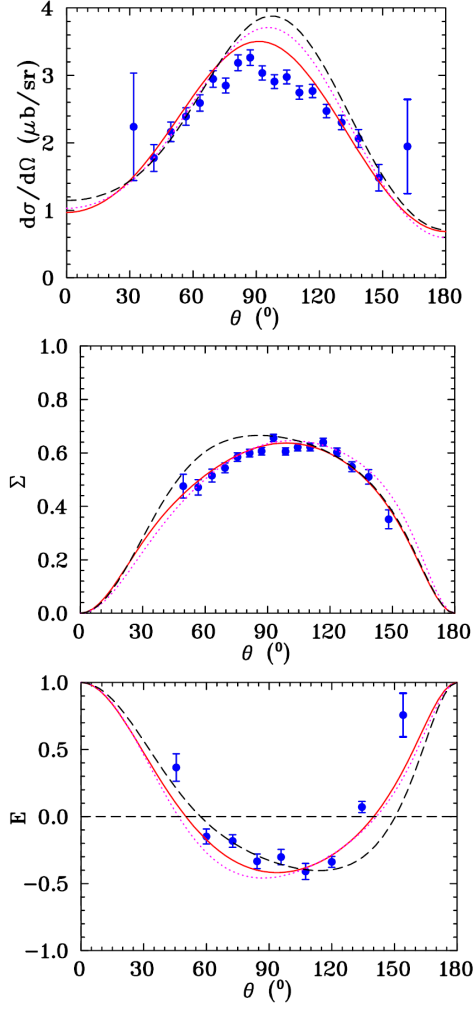


Fig. 8 $d\sigma/d\Omega$, Σ , and E observables for $\vec{\gamma}n \rightarrow \pi^0 n$ (blue full circles). All data were produced by the A2 Collaboration at MAMI: $d\sigma/d\Omega$ at $E_\gamma = 610$ MeV (top) are from Ref. [4], Σ at $E_\gamma = 610$ MeV (middle) are present measurement, and E at $E_\gamma = 603$ MeV (bottom) are from Ref. [11]. New SAID solutions MU22 (MUXX) are shown by red solid (magenta dotted) curves and MAID2007 [29] by black dashed curves.

compared to predictions from MUXX and MAID2007 for $d\sigma/d\Omega$, Σ , and the double-polarization asymmetry E . At this energy, the qualitative features are generally reproduced, particularly for the current data. In the fit, cross sections have larger angle-independent systematic uncertainties and the renormalization factor from Eq. (9) improves the description, but is not included in the plot. While the new data cover parts of the Δ and Roper resonance regions, selected isospin multipoles are compared up to a photon energy of 1 GeV. The isospin 3/2 multipoles are taken as determined by the much larger proton-target database and only the isospin 1/2 neutron multipoles are shown in Fig. 9.

Comparing MA19 to MA22, there are no significant changes seen in the $M_{1-}^{1/2}$ multipole. In addition, comparing imaginary parts of multipoles connected to the nearby $N(1535)$ ($E_{0+}^{1/2}$) and $N(1520)$ ($E_{2-}^{1/2}$ and $M_{2-}^{1/2}$), there is also good agreement between the SAID and Bonn-Gatchina plots. The resonance couplings for the $N(1535)$, $N(1440)$, and $N(1520)$ are expected to be in agreement with those reported in Ref. [4].

As a final comment on the predictive ability of our fit, excluding all $\pi^0 n$ data, a comparison of Tables 4 and 5 shows that fit MUXX is much less successful between the upper energy limit of the present experiment and 1 GeV in the photon energy. This change is due mainly to poor compatibility with GRAAL Σ data [10].

Our results for Σ for $\vec{\gamma}d \rightarrow \pi^0 n(p)$ consist of 189 experimental points and are available from the SAID database [2], where systematic uncertainties for each bin have been added in quadrature.

Acknowledgements This work was supported in part by the UK Science and Technology Facilities Council (STFC Grants No. 57071/1 and No. 50727/1), the U. S. Department of Energy, Office of Science, Office of Nuclear Physics, under Awards No. DE-FG02-01ER41194, No. DE-SC0016583, No. DE-SC0016582, and No. DE-SC0014323. This work was supported by Schweizerischer Nationalfonds (Grants No. 200020-132799, No. 121781, No. 117601, and No. 113511), Deutsche Forschungsgemeinschaft (SFB Grant No. 443, No. SFB/TR 16, No. SFB 1044), DFG-RFBR (Grant No. 05-02-04014), European Community Research Infrastructure Activity (FP6), the U. S. DOE, U. S. NSF, and NSERC (Grant No. SAPPJ-2018-00020) Canada. This publication is part of a project that has received funding from the European Union’s Horizon 2020 research and innovation programme under grant agreement STRONG-2020-No 824093. We would like to thank all the technical and nontechnical staff of MAMI for their support.

References

1. D. G. Ireland, E. Pasyuk, and I. Strakovsky, “Photoproduction reactions and non-strange baryon spectroscopy,” *Prog. Part. Nucl. Phys.* **111**, 103752 (2020).
2. The SAID analyses are available through the GWU web-site <http://gwdac.phys.gwu.edu/>; W. J. Briscoe, M. Döring, H. Haberzettl, I. I. Strakovsky, and R. L. Workman, Institute of Nuclear Studies of The George Washington University Database.
3. K. Kossert *et al.* [A2 Collaboration at MAMI], “Quasifree π^0 photoproduction from the bound nucleon,” *Eur. Phys. J. A* **19**, 391 (2004).
4. W. J. Briscoe *et al.* [A2 Collaboration at MAMI], “Cross section for $\gamma n \rightarrow \pi^0 n$ at the Mainz A2 experiment,” *Phys. Rev. C* **100**, 065205 (2019).
5. A. Ando, in “Physik-Daten, Physics Data,” *Sekt. 7 “Compilation of Pion Photoproduction Data,”* edited by H. Behrens, G. Ebel, D. Menze, W. Pfeil, and R. Wilcke (Physikalisches Institut der Universität, Bonn, Germany, 1977), Vol. 1.

6. M. Dieterle *et al.* [A2 Collaboration at MAMI], “Photoproduction of π^0 mesons off protons and neutrons in the second and third nucleon resonance region,” *Phys. Rev. C* **97**, 065205 (2018). It is not included in the SAID fits due to no FSI corrections while it is available in the SAID database [2].
7. Y. Hemmi *et al.*, “Photoproduction of neutral pions off neutrons in the energy region between 500 MeV and 900 MeV,” *Nucl. Phys. B* **55**, 333 (1973).
8. C. Bacci *et al.* “Angular distributions for single neutral pion photoproduction from neutrons at 450 – 800 MeV,” *Phys. Lett. B* **39**, 559 (1972).
9. C. R. Clinesmith, “ π^0 photoproduction from the deuteron at forward angles in the energy range from 900-MeV to 1400-MeV,” Ph. D. Thesis, California Institute of Technology, 1967; Preprint RX-184.
10. R. Di Salvo *et al.* [GRAAL Collaboration], “Measurement of Sigma beam asymmetry in π^0 photoproduction off the neutron in the second and third resonances region,” *Eur. Phys. J. A* **42**, 151 (2009).
11. M. Dieterle *et al.* [A2 Collaboration at MAMI], “First measurement of the polarization observable E and helicity-dependent cross sections in single π^0 photoproduction from quasi-free nucleons,” *Phys. Lett. B* **770**, 523 (2017).
12. S. Costanza and F. Cividini, “Double polarization observable E and helicity dependent cross section for single π^0 photoproduction off proton and neutron,” *EPJ Web Conf.* **241**, 01005 (2020).
13. V. E. Tarasov, W. J. Briscoe, H. Gao, A. E. Kudryavtsev, and I. I. Strakovsky, “Extracting the photoproduction cross section off the neutron $\gamma n \rightarrow \pi^- p$ from deuteron data with FSI effects,” *Phys. Rev. C* **84**, 035203 (2011).
14. P. T. Mattione *et al.* [CLAS Collaboration], “Differential cross section measurements for $\gamma n \rightarrow \pi^- p$ above the first nucleon resonance region,” *Phys. Rev. C* **96**, 035204 (2017).
15. V. E. Tarasov, W. J. Briscoe, M. Dieterle, B. Krusche, A. E. Kudryavtsev, M. Ostrick, and I. I. Strakovsky, “On the extraction of cross sections for π^0 and η photoproduction off neutrons from deuteron data,” *Phys. Atom. Nucl.* **79**, 216 (2016).
16. J. C. McGeorge *et al.*, “Upgrade of the Glasgow photon tagging spectrometer for Mainz MAMI-C,” *Eur. Phys. J. A* **37**, 129 (2008).
17. A. Starostin *et al.* [Crystal Ball Collaboration], “Measurement of $K^- p \rightarrow \eta \Lambda$ near threshold,” *Phys. Rev. C* **64**, 055205 (2001).
18. A. R. Gabler *et al.*, “Response of TAPS to monochromatic photons with energies between 45-MeV and 790-MeV,” *Nucl. Instrum. Meth. A* **346**, 168 (1994).
19. M. Bashkanov *et al.* [A2 Collaboration at MAMI], “Signatures of the $d^*(2380)$ hexaquark in $d(\gamma, p \vec{\pi}^0)$,” *Phys. Rev. Lett.* **124**, 132001 (2020).
20. C. A. Mullen, “Linearly polarised pion photoproduction on the deuteron,” Ph. D. Thesis, Glasgow University, 2020.
21. D. Lohmann *et al.* “Linearly polarized photons at MAMI (Mainz),” *Nucl. Instrum. Meth. A* **343**, 494 (1994).
22. U. Timm, “Coherent bremsstrahlung of electrons in crystals,” *Fortsch. Phys.* **17**, 765 (1969).
23. J. D. Kellie *et al.*, “The selection and performance of diamond radiators used in coherent bremsstrahlung experiments,” *Nucl. Instrum. Meth. A* **545**, 164 (2005).
24. K. Livingston, “The Stonehenge Technique. A new method for aligning coherent bremsstrahlung radiators,” *Nucl. Instrum. Meth. A* **603**, 205 (2009).
25. S. Gardner *et al.* [A2 Collaboration at MAMI], “Photon asymmetry measurements of $\vec{\gamma} p \rightarrow \pi^0 p$ for $E_\gamma = 320 - 650$ MeV,” *Eur. Phys. J. A* **52**, 333 (2016).
26. M. Pivk and F. R. Le Diberder, “SPlot: A Statistical tool to unfold data distributions,” *Nucl. Instrum. Meth. A* **555**, 356 (2005).
27. W. Verkerke and D. P. Kirkby, “The RooFit toolkit for data modeling,” *eConf C0303241*, MOLT007 (2003).
28. The Bonn-Gatchina analyses are available through the Bonn website: <http://pwa.hiskp.uni-bonn.de/> ; see also E. Gutz *et al.* [CBELSA/TAPS Collaboration], “High statistics study of the reaction $\gamma p \rightarrow p \pi^0 \eta$,” *Eur. Phys. J. A* **50**, 74 (2014).
29. The MAID analyses are available through the Mainz website: <http://wwwkph.kph.uni-mainz.de/MAID/> ; see also D. Drechsel, S. S. Kamalov, and L. Tiator, “Unitary isobar model - MAID2007,” *Eur. Phys. J. A* **34**, 69 (2007).
30. R. L. Workman, M. W. Paris, W. J. Briscoe, and I. I. Strakovsky, “Unified Chew-Mandelstam SAID analysis of pion photoproduction data,” *Phys. Rev. C* **86**, 015202 (2012).
31. A. V. Anisovich, E. Klempt, V. A. Nikonov, M. A. Matveev, A. V. Sarantsev, and U. Thoma, “Photoproduction of pions and properties of baryon resonances from a Bonn-Gatchina partial wave analysis,” *Eur. Phys. J. A* **44**, 203 (2010).
32. R. A. Arndt, W. J. Briscoe, I. I. Strakovsky, and R. L. Workman, “Extended partial-wave analysis of πN scattering data,” *Phys. Rev. C* **74**, 045205 (2006).
33. S. Agostinelli *et al.* “Geant4—a simulation toolkit” *Nucl. Instrum. Meth. A* **506**, 250-303 (2003).

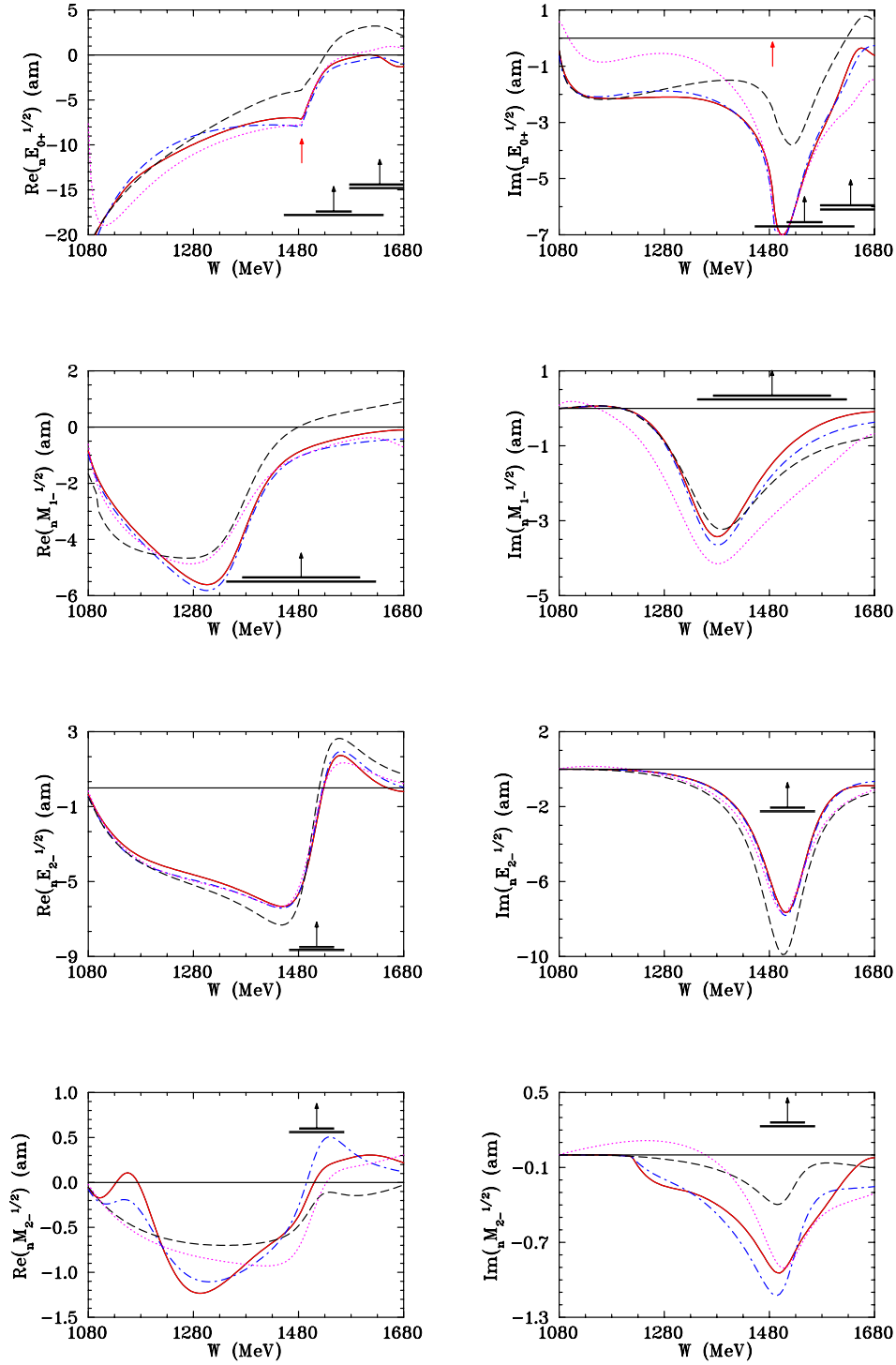


Fig. 9 Selected neutron multipole $I = 1/2$ amplitude from threshold to $W = 1.68$ GeV ($E_\gamma = 1030$ MeV) for the states 0^+ , 1^- , and 2^- . The blue dash-dotted (red solid) curves correspond to the SAID MA19 [4] (new MU22 including present A2 data) solution. The magenta dotted (black dashed) curves give the Bonn-Gatchina BG2014-02 [28] (MAID2007 [29]). The vertical black arrows indicate Breit-Wigner (BW) mass (W_R), and horizontal bars show full (Γ) and partial ($\Gamma_{\pi N}$) widths of resonances extracted by the BW fit of the πN data associated with the SAID solution SP06 [32]. Vertical red arrows show the η meson production threshold.

Insert your title here^{*}

Do you have a subtitle?

If so, write it here

First Author^{a,1}, Second Author^{b,2,3}

¹First Address, Street, City, Country

²Second Address, Street, City, Country

³Present Address: Street, City, Country

Received: date / Accepted: date

Abstract Insert your abstract here. Insert your abstract here. Insert your abstract here. Insert your abstract here. Insert your abstract here. Insert your abstract here. Insert your abstract here. Insert your abstract here. Insert your abstract here.

1 Ordinary text

The ends of words and sentences are marked by spaces. It doesn't matter how many spaces you type; one is as good as 100. The end of a line counts as a space.

One or more blank lines denote the end of a paragraph.

Since any number of consecutive spaces are treated like a single one, the formatting of the input file makes no difference to \LaTeX , but it makes a difference to you. When you use \LaTeX , making your input file as easy to read as possible will be a great help as you write your document and when you change it. This sample file shows how you can add comments to your own input file.

Because printing is different from typewriting, there are a number of things that you have to do differently when preparing an input file than if you were just typing the document directly. Quotation marks like “this” have to be handled specially, as do quotes within quotes: “‘this’ is what I just wrote, not ‘that’”.

Dashes come in three sizes: an intra-word dash, a medium dash for number ranges like 1–2, and a punctuation dash—like this.

A sentence-ending space should be larger than the space between words within a sentence. You sometimes have to type special commands in conjunction with punctuation characters to get this right, as in the following sentence. Gnats,

^{*}Thanks to the title

^ae-mail: magic1@xxx.xx

^be-mail: magic2@xxx.xx

gnus, etc. all begin with G. You should check the spaces after periods when reading your output to make sure you haven't forgotten any special cases. Generating an ellipsis ... with the right spacing around the periods requires a special command.

\TeX interprets some common characters as commands, so you must type special commands to generate them. These characters include the following: & % # { and }.

In printing, text is emphasized by using an *italic* type style.

A long segment of text can also be emphasized in this way. Text within such a segment given additional emphasis with Roman type. Italic type loses its ability to emphasize and become simply distracting when used excessively.

It is sometimes necessary to prevent \TeX from breaking a line where it might otherwise do so. This may be at a space, as between the “Mr.” and “Jones” in “Mr. Jones”, or within a word—especially when the word is a symbol like *itemnum* that makes little sense when hyphenated across lines.

\TeX is good at typesetting mathematical formulas like $x - 3y = 7$ or $a_1 > x^{2n}/y^{2n} > x'$. Remember that a letter like x is a formula when it denotes a mathematical symbol, and should be treated as one.

2 Notes

Footnotes¹ pose no problem.²

3 Displayed text

Text is displayed by indenting it from the left margin. Quotations are commonly displayed. There are short quotations

¹This is an example of a footnote.

²And another one.

This is a short a quotation. It consists of a single paragraph of text. There is no paragraph indentation. and longer ones.

This is a longer quotation. It consists of two paragraphs of text. The beginning of each paragraph is indicated by an extra indentation.

This is the second paragraph of the quotation. It is just as dull as the first paragraph.

Another frequently-displayed structure is a list. The following is an example of an *itemized* list, four levels deep.

- This is the first item of an itemized list. Each item in the list is marked with a “tick”. The document style determines what kind of tick mark is used.
- This is the second item of the list. It contains another list nested inside it. The three inner lists are an *itemized* list.
 - This is the first item of an enumerated list that is nested within the itemized list.
 - This is the second item of the inner list. \LaTeX allows you to nest lists deeper than you really should.

This is the rest of the second item of the outer list. It is no more interesting than any other part of the item.
- This is the third item of the list.

The following is an example of an *enumerated* list, four levels deep.

1. This is the first item of an enumerated list. Each item in the list is marked with a “tick”. The document style determines what kind of tick mark is used.
2. This is the second item of the list. It contains another list nested inside it. The three inner lists are an *enumerated* list.
 - (a) This is the first item of an enumerated list that is nested within the enumerated list.
 - (b) This is the second item of the inner list. \LaTeX allows you to nest lists deeper than you really should.

This is the rest of the second item of the outer list. It is no more interesting than any other part of the item.
3. This is the third item of the list.

The following is an example of a *description* list.

Cow Highly intelligent animal that can produce milk out of grass.

Horse Less intelligent animal renowned for its legs.

Human being Not so intelligent animal that thinks that it can think.

You can even display poetry.

There is an environment for verse
Whose features some poets will curse.
For instead of making
Them do *all* line breaking,
It allows them to put too many words on a line when
they’d rather be forced to be terse.

Mathematical formulas may also be displayed. A displayed formula is one-line long; multiline formulas require special formatting instructions.

$$x' + y^2 = z_i^2$$

Don’t start a paragraph with a displayed equation, nor make one a paragraph by itself.

Example of a theorem:

Lemma 1 *All conjectures are interesting, but some conjectures are more interesting than others.*

Proof Obvious. □

4 Tables and figures

Cross reference to labelled table: As you can see in Table 1 on page 3 and also in Table 2 on page 3.

A major point of difference lies in the value of the specific production rate π for large values of the specific growth rate μ . Already in the early publications [1–3] it appeared that high glucose concentrations in the production phase are well correlated with a low penicillin yield (the ‘glucose effect’). It has been confirmed recently [1–4] that high glucose concentrations inhibit the synthesis of the enzymes of the penicillin pathway, but not the actual penicillin biosynthesis. In other words, glucose represses (and not inhibits) the penicillin biosynthesis.

These findings do not contradict the results of [1] and of [4] which were obtained for continuous culture fermentations. Because for high values of the specific growth rate μ it is most likely (as shall be discussed below) that maintenance metabolism occurs, it can be shown that in steady state continuous culture conditions, and with μ described by a Monod kinetics

$$C_s = K_M \frac{\mu / \mu_x}{1 - \mu / \mu_x} \quad (1)$$

Pirt and Rhigelato determined π for μ between 0.023 and 0.086 h⁻¹. They also reported a value $\mu_x \approx 0.095$ h⁻¹, so that for their experiments μ / μ_x is in the range of 0.24 to 0.9. Substituting K_M in (1) by the value $K_M = 1$ g/L as used by [1], one finds with the above equation $0.3 < C_s < 9$ g/L. This agrees well with the work of [4], who reported that penicillin biosynthesis repression only occurs at glucose concentrations from $C_s = 10$ g/L on. The conclusion is that the glucose concentrations in the experiments of Pirt and Rhigelato probably were too low for glucose repression to be detected. The experimental data published by Ryu and Hospodka are not detailed sufficiently to permit a similar analysis.

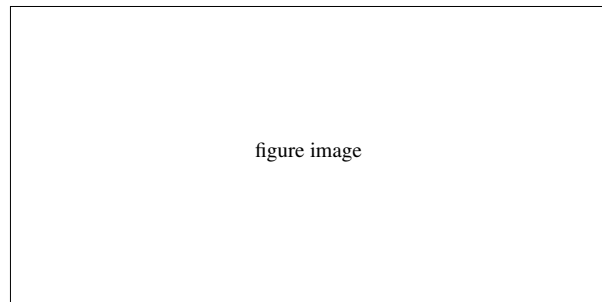
Bajpai and Reuß decided to disregard the differences between time constants for the two regulation mechanisms (glucose repression or inhibition) because of the relatively

Table 1 The spherical case ($I_1 = 0, I_2 = 0$)

Equil. Points	x	y	z	C	S
L_1	-2.485252241	0.000000000	0.017100631	8.230711648	U
L_2	0.000000000	0.000000000	3.068883732	0.000000000	S
L_3	0.009869059	0.000000000	4.756386544	-0.000057922	U
L_4	0.210589855	0.000000000	-0.007021459	9.440510897	U
L_5	0.455926604	0.000000000	-0.212446624	7.586126667	U
L_6	0.667031314	0.000000000	0.529879957	3.497660052	U
L_7	2.164386674	0.000000000	-0.169308438	6.866562449	U
L_8	0.560414471	0.421735658	-0.093667445	9.241525367	U
L_9	0.560414471	-0.421735658	-0.093667445	9.241525367	U
L_{10}	1.472523232	1.393484549	-0.083801333	6.733436505	U
L_{11}	1.472523232	-1.393484549	-0.083801333	6.733436505	U

Table 2 Parameter sets used by Bajpai and Reuß

parameter		Set 1	Set 2
μ_x	[h ⁻¹]	0.092	0.11
K_x	[g/g DM]	0.15	0.006
μ_p	[g/g DM h]	0.005	0.004
K_p	[g/L]	0.0002	0.0001
K_i	[g/L]	0.1	0.1
$Y_{x/s}$	[g DM/g]	0.45	0.47
$Y_{p/s}$	[g/g]	0.9	1.2
k_h	[h ⁻¹]	0.04	0.01
m_s	[g/g DM h]	0.014	0.029

**Fig. 1** Pathway of the penicillin G biosynthesis

very long fermentation times, and therefore proposed a Haldane expression for π .

It is interesting that simulations with the [4] model for the initial conditions given by these authors indicate that, when the remaining substrate is fed at a constant rate, a considerable and unrealistic amount of penicillin is produced when the glucose concentration is still very high [2–4]. Simulations with the Bajpai and Reuß model correctly predict almost no penicillin production in similar conditions.

Sample of cross-reference to figure. Figure 1 shows that is not easy to get something on paper.

5 Headings

5.1 Subsection

Carr-Goldstein based their model on balancing methods and biochemical knowledge. The original model (1980) contained an equation for the oxygen dynamics which has been omitted in a second paper (1981). This simplified model shall be discussed here.

5.1.1 Subsubsection

Carr-Goldstein based their model on balancing methods and biochemical knowledge. The original model (1980) contained an equation for the oxygen dynamics which has been omitted in a second paper (1981). This simplified model shall be discussed here.

6 Equations and the like

Two equations:

$$C_s = K_M \frac{\mu/\mu_x}{1 - \mu/\mu_x} \quad (2)$$

and

$$G = \frac{P_{\text{opt}} - P_{\text{ref}}}{P_{\text{ref}}} 100 (\%) \quad (3)$$

Two equation arrays:

$$\frac{dS}{dt} = -\sigma X + s_F F \quad (4)$$

$$\frac{dX}{dt} = \mu X \quad (5)$$

$$\frac{dP}{dt} = \pi X - k_h P \quad (6)$$

$$\frac{dV}{dt} = F \quad (7)$$

and,

$$\mu_{\text{substr}} = \mu_x \frac{C_s}{K_x C_x + C_s} \quad (8)$$

$$\mu = \mu_{\text{substr}} - Y_{x/s}(1 - H(C_s))(m_s + \pi/Y_{p/s}) \quad (9)$$

$$\sigma = \mu_{\text{substr}}/Y_{x/s} + H(C_s)(m_s + \pi/Y_{p/s}) \quad (10)$$

Acknowledgements If you'd like to thank anyone, place your comments here and remove the percent signs.

Appendix A: Appendix section

We consider a sequence of queueing systems indexed by n . It is assumed that each system is composed of J stations, indexed by 1 through J , and K customer classes, indexed by 1 through K . Each customer class has a fixed route through the network of stations. Customers in class k , $k = 1, \dots, K$, arrive to the system according to a renewal process, independently of the arrivals of the other customer classes. These customers move through the network, never visiting a station more than once, until they eventually exit the system.

Appendix subsection

However, different customer classes may visit stations in different orders; the system is not necessarily “feed-forward.” We define the *path of class k customers* in as the sequence of servers they encounter along their way through the network and denote it by

$$\mathcal{P} = (j_{k,1}, j_{k,2}, \dots, j_{k,m(k)}). \quad (\text{A.1})$$

Sample of cross-reference to the formula (A.1) in [Appendix A](#).

Appendix B: Appendix section

We consider a sequence of queueing systems indexed by n . It is assumed that each system is composed of J stations, indexed by 1 through J , and K customer classes, indexed by 1 through K . Each customer class has a fixed route through the network of stations. Customers in class k , $k = 1, \dots, K$, arrive to the system according to a renewal process, independently of the arrivals of the other customer classes. These customers move through the network, never visiting a station more than once, until they eventually exit the system.

References

1. S. Chekanov et al. (ZEUS Collaboration), Eur. Phys. J. C **42**, 1 (2005)
2. P.C. Brans, U.G. Meissner, Eur. Phys. J. C **40**, 97 (2005)
3. N. Kersting, Eur. Phys. J. C (2009). doi:10.1140/epjc/s10052-009-1063-6
4. J.M. Smith, *Molecular Dynamics*, 2nd edn. (Springer, Berlin, Heidelberg, 1987)
5. J.M. Smith, in *Molecular Dynamics*, ed. by C. Brown, 2nd edn. (Les Editions de Physique, Les Ulis, 1987)
6. J.M. Smith, in *Molecular Dynamics*, ed. by C. Brown, 2nd edn. (Springer, Berlin, Heidelberg, 2009 in press)
7. J.M. Smith, in *Proceedings of the International Conference on Low Temperature Physics, Madison, 1975*, ed. by C. Brown (Les Éditions de Physique, Les Ulis, 1975), p. 201
8. J. Cartwright, Big stars have weather too. (IOP Publishing PhysicsWeb, 2007), <http://physicsweb.org/articles/news/11/6/16/1>. Accessed 26 June 2007